Multi-spacecraft Observations of the Coronal and Interplanetary Evolution of a Solar Eruption Associated with Two Active Regions

Huidong Hu[1,2], Ying D. Liu[1,2], Rui Wang[1], Xiaowei Zhao[1,2], Bei Zhu[1,2], and Zhongwei Yang[1]
[1] State Key Laboratory of Space Weather, National Space Science Center, Chinese Academy of Sciences, Beijing 100190, China; liuxying@spaceweather.ac.cn
[2] University of Chinese Academy of Sciences, Beijing 100049, China

Abstract

We investigate the coronal and interplanetary evolution of a coronal mass ejection (CME) launched on 2010 September 4 from a source region linking two active regions (ARs), 11101 and 11103, using extreme ultraviolet imaging, magnetogram, white-light, and in situ observations from *SDO*, *STEREO*, *SOHO*, *VEX*, and *Wind*. A potential-field source-surface model is employed to examine the configuration of the coronal magnetic field surrounding the source region. The graduated cylindrical shell model and a triangulation method are applied to determine the kinematics of the CME in the corona and interplanetary space. From the remote sensing and in situ observations, we obtain some key results: (1) the CME was deflected in both the eastward and southward directions in the low corona by the magnetic pressure from the two ARs, and possibly interacted with another ejection, which caused that the CME arrived at *VEX* that was longitudinally distant from the source region; (2) although *VEX* was closer to the Sun, the observed and derived CME arrival times at *VEX* are not earlier than those at *Wind*, which suggests the importance of determining both the frontal shape and propagation direction of the CME in interplanetary space; and (3) the ICME was compressed in the radial direction while the longitudinal transverse size was extended.

Key words: solar–terrestrial relations – solar wind – Sun: activity – Sun: coronal mass ejections (CMEs) – Sun: magnetic fields

1. Introduction

Coronal mass ejections (CMEs) are large expulsions of plasma and rapid releases of magnetic field energy from the solar atmosphere. They are called interplanetary CMEs (ICMEs) when propagating in interplanetary space, and are one of the major disturbances in the solar wind. ICMEs are also significant factors inducing geomagnetic activities when they impact the Earth. From the low corona to interplanetary space, a CME may experience non-radial motion, interact with other CMEs, and be deformed due to the interaction with the ambient solar wind, involving plenty of physical processes.

The configuration of the magnetic field surrounding the source region as well as the interaction with other structures in the solar wind are important for estimating the propagation direction of a CME and thus crucial for space weather forecasting. Previous coronagraph observations suggested that latitudinal deflections of CMEs were controlled by the background coronal magnetic field and the overall flow near solar minimum (MacQueen et al. 1986), which was confirmed by the result that CMEs near solar minimum were systematically deflected toward lower latitudes, while CMEs during solar maximum could deviate toward either the pole or the equator (e.g., Cremades & Bothmer 2004; Kilpua et al. 2009). Some CMEs were found to be deflected toward the weak magnetic field region associated with the streamer belt or the heliospheric current sheet (e.g., Xie et al. 2009; Kay et al. 2013; Liewer et al. 2015), while Xie et al. (2009) reported that fast CMEs could be deflected away from the streamer belt. The coronal hole with strong open magnetic field is one important factor that can divert a CME (e.g., Gopalswamy et al. 2004, 2005, 2009; Xie et al. 2009; Panasenco et al. 2013). Möstl et al. (2015) and Wang et al. (2015) found that the strong magnetic field of a sunspot in an active region (AR) and the configurations of the magnetic field surrounding the source region play a significant role in channeling the CME. The deflection of CMEs in the corona is likely to occur within a few solar radii from the Sun (e.g., Isavnin et al. 2014; Kay et al. 2015; Wang et al. 2015), while CME–CME interaction may change the propagation direction of a CME in interplanetary space (e.g., Gopalswamy et al. 2001; Liu et al. 2012, 2014; Lugaz et al. 2012).

A plethora of efforts have been made to understand the morphology of the CME in the corona and interplanetary space, which is crucial to determine the arrival time of the CME at a planet. Thernisien et al. (2006, 2009) presented the graduated cylindrical shell (GCS) model employing a croissant-like empirical flux-rope structure to describe the morphology of the CME near the Sun. A compact structure was used to derive CME kinematics (e.g., Sheeley et al. 1999). A circle attached to the Sun, called the harmonic mean (HM) method, was also applied to determine the kinematics in the inner heliosphere (e.g., Lugaz et al. 2009). A self-similar expansion geometry with an expanding circle in the ecliptic plane was adopted to describe the CME front (Lugaz et al. 2010; Davies et al. 2012; Möstl & Davies 2013). Möstl et al. (2015) and Rollett et al. (2016) introduced an elliptical shape with a constant angular width to forecast CME arrival time and speed based on single-viewpoint imaging observations. The readers are directed to Liu et al. (2010b) for discussions of some of the geometries. However, a CME could be deformed by interacting with the ambient solar wind (e.g., Riley et al. 2003; Manchester et al. 2004; Odstrcil et al. 2004; Liu et al. 2006; Savani et al. 2010), as well as structures in the solar wind (e.g., Lugaz et al. 2009; Liu et al. 2012, 2015; Kataoka et al. 2015). These interactions can alter their plasma and magnetic field characteristics as well as morphologies in interplanetary space.
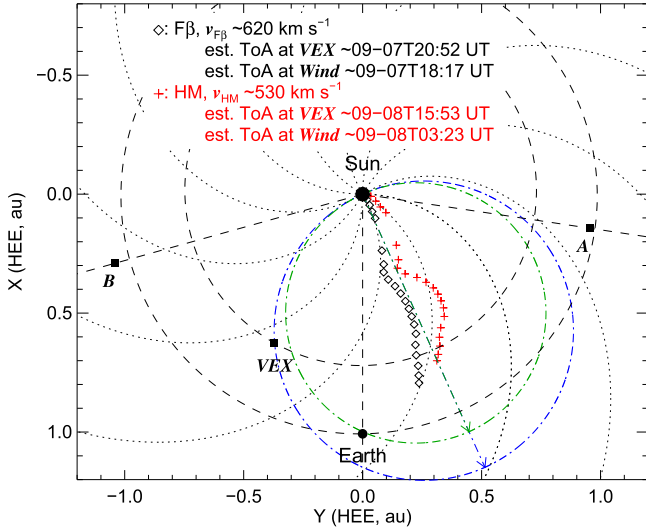
Figure 1. Positions of *VEX*, *STEREO A*, *STEREO B*, and the Earth in the ecliptic plane on 2010 September 8. The trajectories of the apex of the CME are derived from the triangulation method with the Fβ (black diamond) and HM (red cross) approximations, respectively. The green (blue) circle represents the size of the assumed spherical CME front when arriving at *Wind* (*VEX*), and the green (blue) arrow indicates the direction of the CME apex then. The black circles mark the orbits of *VEX*, and the Earth, respectively, and the gray dotted curves show Parker spiral magnetic field lines created with a solar wind speed of 450 km s^{-1}. The average speeds of the CME as well as the estimated arrival times at *VEX* and *Wind* from the two approximations are also given.

In this paper, we investigate the coronal and interplanetary evolution of a CME launched from a source region linking two ARs. The eruption may occur as a result of magnetic coupling of the two ARs, but it is different from the cases of sympathetic eruptions (e.g., Schrijver & Title 2011; Jin et al. 2016). The remote sensing and in situ observations from *SDO*, *STEREO*, *SOHO*, *VEX*, and *Wind* are used in this study. The positions of the spacecraft and planets during the event are indicated in Figure 1. *STEREO A* was ~81° ahead of the Earth and was ~20° west of the source region (~W62°), and *STEREO B* was ~74° behind the Earth. *VEX* (Venus) was ~0.73 au from the Sun and ~31° east of the Earth. The spacecraft are at positions that are advantageous for investigating the kinematics and the structure of the CME. This study illustrates how the magnetic field of the two ARs on one side of the source region change the motion of the CME near the Sun. The multi-spacecraft in situ measurements and remote sensing observations place constraints on the structure and the kinematics of the CME, and demonstrate how the frontal shape and propagation direction determine the arrival time of the CME. Furthermore, multiple spacecraft at longitudinally separated positions reveal the longitudinal transverse size of the ICME, which is important for understanding the structure and distortion of the ICME in the solar wind. The evolution of the CME in the corona and interplanetary space is presented in Sections 2 and 3, respectively. We conclude and discuss the results in Section 4. The results of this work shed light on the kinematics and morphological evolution of the CME in the inner heliosphere as well as space weather forecasting.

2. Evolution in the Corona

The CME was launched around 14:30 UT on 2010 September 4 in the rising phase of solar cycle 24, associated with two roughly straight flare ribbons on the eastern edges of
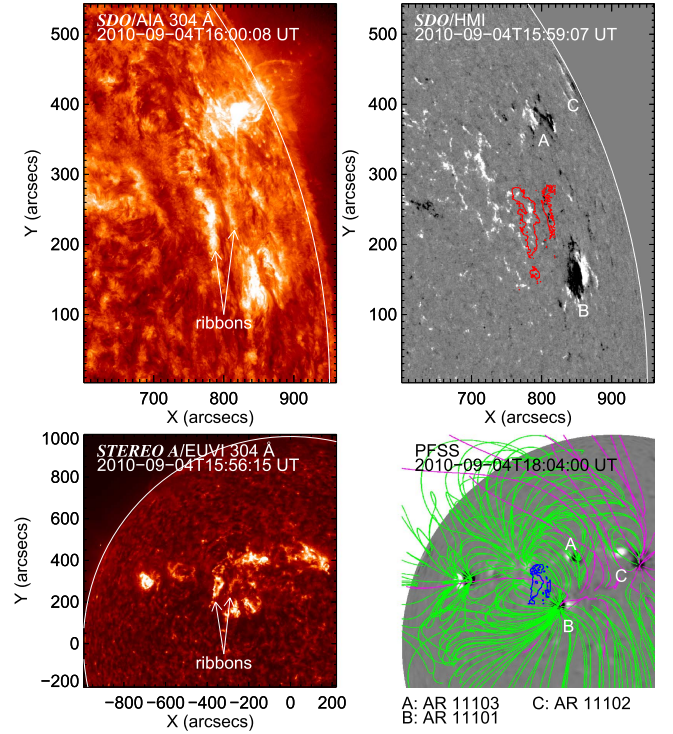

Figure 2. EUV observations and magnetic field conditions of the CME source regions. Upper left: EUV image at wavelength 304 Å from *SDO*/AIA showing the two ribbons associated with the CME. Upper right: line-of-sight magnetogram from *SDO*/HMI with an overlaid AIA 304 Å intensity contour of the two ribbons (red closed curves). Lower left: EUV image at wavelength 304 Å from *STEREO A*/EUVI. Lower right: PFSS modeled magnetic field surrounding the source region from the viewpoint of *STEREO A*, where the green lines represent the closed field lines, and the purple lines are the open magnetic field lines; the overlaid blue closed curves are a *STEREO A*/EUVI 304 Å intensity contour indicating the positions of the two ribbons. The locations of the flare ribbons are marked in the EUV images. ARs 11103, 11101, and 11102 are indicated with "A," "B," and "C," respectively, in the magnetograms. The white (dark) regions in the magnetograms represent the positive (negative) magnetic field regions.

two ARs 11101 (W67°N11°) and 11103 (W69°N26°), as shown in the right panel of Figure 2. Figure 2 displays the extreme ultraviolet (EUV) images and magnetograms about the source region from *SDO* and *STEREO A*. In the magnetograms, the white (dark) regions represent the positive (negative) magnetic field regions, and the locations of ARs 11103, 11101, and 11102 are marked with "A," "B," and "C," respectively. According to the EUV observations of *SDO*/AIA (Lemen et al. 2012) and *STEREO A*/EUVI (Howard et al. 2008), the ribbons became visible at wavelength 304 Å at about 14:16 UT and separated eastward and westward, respectively. From the *SDO*/HMI (Schou et al. 2012) magnetogram overlaid with the intensity contour of the AIA 304 Å image, the magnetic field corresponding to the eastern ribbon is positive and the magnetic field for the western ribbon is negative. The neutral line between the two ribbons is along the meridian and at a longitude of ~W62° (~77° in Carrington longitudes). Viewing from the viewpoint of *STEREO A*, a potential-field source-surface (PFSS) model reveals an overlying loop structure above the two flare ribbons as shown in the lower right panel of Figure 2. The associated loop brightening during the eruption was also observed at wavelength 195 Å by *STEREO A*/EUVI (not shown here). A hot channel, which is considered as an erupting flux rope (e.g., Zhang et al. 2012; Cheng et al. 2014),
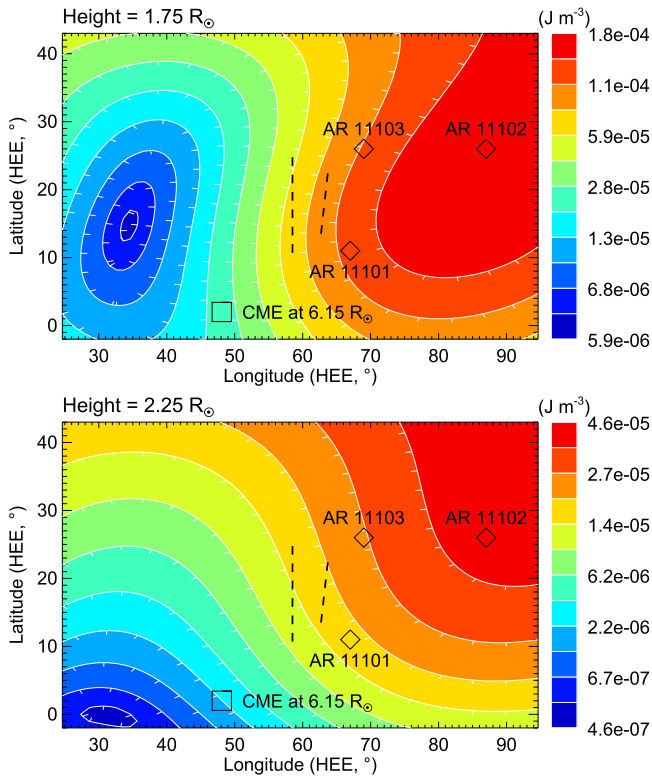
Figure 3. Contours of the magnetic energy density at heights of 1.75 $R_\odot$ (upper panel) and 2.25 $R_\odot$ (lower panel) from the PFSS extrapolation. The two vertical dashed lines indicate the approximate positions of the two ribbons determined from the *STEREO A*/EUVI 304 Å image. The diamonds mark the positions of ARs 11103, 11101, and 11102, respectively. The square symbol represents the propagation direction at the height of 6.15 $R_\odot$ determined by the GCS model (see the text).

is not observed in the EUV images. However, an eruption with a two-ribbon flare and loop brightening is considered to be evidence of an erupting flux rope (e.g., Amari et al. 2000; Qiu et al. 2004). In our case, an erupting flux rope could be inferred from the flare ribbons and the loop brightening, which was lying over the neutral line between the two ribbons. The erupting flux rope probably was of low twist because the magnetic field near the neutral line was relatively weak and not strongly sheared. As can be inferred from the combined EUV and HMI observations in the upper right panel of Figure 2, the erupting flux rope likely extended from the positive polarity region of AR 11103 (marked with "A") in the north to the negative polarity region of AR 11101 (marked with "B") in the south. The source region of the CME was expected to be between the two ribbons and adjacent to the eastern edges of the two ARs. ARs 11103 and 11101 are separated by ~15° in latitudes, but may be connected through the erupting flux rope that is under the PFFS model revealed loop structure. The maximum magnitude of the HMI measured magnetic field in AR 11101 is about 2100 Gauss, and the one in AR 11103 is about 1600 Gauss. Möstl et al. (2015) and Wang et al. (2015) reported that the strong magnetic field (over 3000 Gauss) of a nearby sunspot could change the propagation direction of the CME near the Sun. In our case, although the magnetic field is not so high, the asymmetric magnetic field configuration close to the source region may also interfere the motion of the CME in the corona.

Figure 3 shows the magnetic energy density distribution surrounding the CME source region at heights of 1.75 and

2.25 $R_\odot$. The magnetic energy density w_B is calculated from $w_B = \boldsymbol{B}^2/2\mu_0$, where the magnetic field $\boldsymbol{B}$ is from the PFSS extrapolation and μ_0 is the vacuum permeability. In Figure 3, the two vertical dashed lines indicate the approximate positions of the two ribbons, and the source region is between them. For the sake of simplicity, we use contours of the magnetic energy density to infer the general direction of the gradient descent. As displayed in the upper panel of Figure 3, the contour reveals that the gradient descent of the magnetic energy density near the source region is generally eastward at the height of 1.75 $R_\odot$. As shown in the lower panel of the figure, the gradient descent near the source region at the height of 2.25 $R_\odot$ has a southward component. ARs 11103, 11101, and 11102 marked with diamond symbols in Figure 3 are generally in the regions of higher magnetic energy density on the west side of the source region. This implies that ARs 11103, 11101, and possibly 11102 caused an asymmetric magnetic field configuration near the source region. Previous studies suggested that an asymmetric configuration of the coronal magnetic field could deflect a CME toward the weak magnetic field region (e.g., MacQueen et al. 1986; Kilpua et al. 2009; Kay et al. 2015; Wang et al. 2015). We use the GCS model developed by Thernisien et al. (2006, 2009) to investigate the propagation direction near the Sun, and find that the propagation direction of the CME at 6.15 $R_\odot$ (marked with a square in Figure 3) is in the southeast of the source region, which is consistent with the general direction of the gradient descent of the magnetic energy density. The GCS modeling will be detailed in the text below.

The GCS model can determine the height, direction, and other parameters of the CME in the corona based on the coronagraph observations from *STEREO*/SECCHI (Howard et al. 2008) and *SOHO*/LASCO (Domingo et al. 1995). Two coronagraphs are on board each *STEREO* spacecraft (Kaiser et al. 2008), of which COR1 has a field of view (FOV) of 1.5–4 $R_\odot$ and COR2 has a FOV of 2.5–15 $R_\odot$ (Howard et al. 2008). Coronagraph C2 on board *SOHO* has a FOV of 1.5–6 $R_\odot$ and C3 has a FOV of 3–30 $R_\odot$ (Domingo et al. 1995). Multi-spacecraft coronagraph observations from three viewpoints place strong constraints on the parameters of the GCS model. The CME appeared in the FOV of *STEREO B*/COR1 at 15:05 UT, *SOHO*/C2 (from position angle PA ~ 270°) at 15:12 UT, and *STEREO A*/COR1 at 15:37 UT. Running difference coronagraph images from *SOHO*, *STEREO A* and *B* as shown in Figure 4 are used to fit the GCS model parameters of the CME. In every two rows of Figure 4, two sets of identical running difference images are presented, where the GCS modeled CME (green grids) are superimposed on the second set of images. In the running difference images of the top two rows of the figure, we see that the CME was about to enter the FOV of *STEREO A*/COR1 at 15:25 UT when it was clearly observed by *STEREO B*/COR1 and *SOHO*/C2. This strongly restricts the CME propagation direction at that moment with the GCS model because an underestimated angle between the Sun–Earth line and the propagation direction will bring the modeled CME (the green grids) into the FOV of *STEREO A*/COR1 then. In the middle two rows of Figure 4, the running difference image of *SOHO*/C2 shows a loop-like structure in the northwest of the CME. This structure may be a substructure of the CME, and it is not fitted during the GCS model. However, the possibility that the loop-like structure is of another CME cannot be excluded. The front of the CME was distorted and the southern part moved faster than the part above
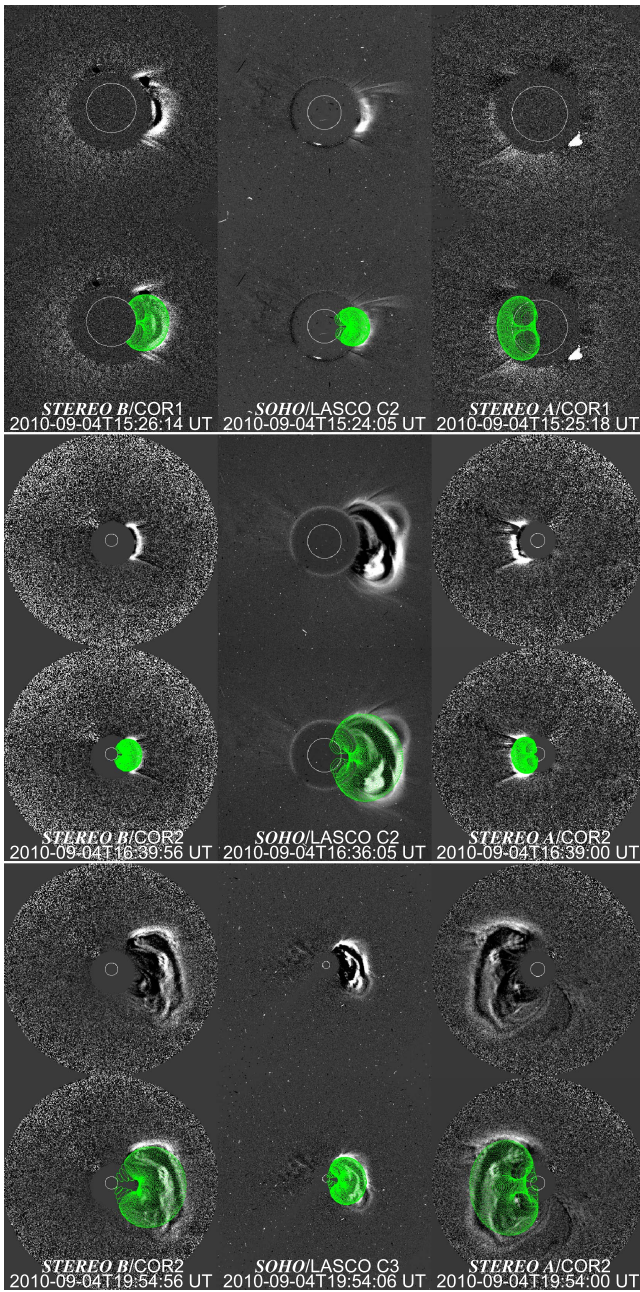
Figure 4. Running difference coronagraph images and corresponding GCS modeling (green grids) from *STEREO B* (left column), *SOHO* (middle column), and *STEREO A* (right column). Detectors and times are stamped in the images.

the ecliptic plane, as displayed in the images of the bottom two rows of Figure 4. The distortion cannot be fitted by changing the tilt-angle parameter of the GCS model. Only the part of the CME front near and above the ecliptic plane is fitted by the GCS model when the distortion is significant. The distortion may be caused by a streamer interacting with the southern part of the CME from the behind, which can be seen in *STEREO*/COR2 white-light observations (not shown here). At each time, tilt-angle, aspect-ratio, half-angle, and latitude parameters of the GCS model are fixed while only the longitude and height parameters are fitted.

The fitted parameters of the GCS model and their corresponding times are given in Table 1. The propagation direction of the CME at height $3.00\,R_{\odot}$ obtained from the GCS

model was $60^{\circ}.4$ west of the Sun–Earth line. It was close to the longitude ($\sim$W62°) of the source region estimated from the EUV and HMI observations. The angle between the propagation direction and the Sun–Earth line decreased remarkably to $48^{\circ}.1$ when the CME height reached $6.15\,R_{\odot}$, and then gradually changed to $45^{\circ}.8$ when the height was $17.57\,R_{\odot}$. During the whole GCS process, the tilt-angle parameter is set to 90°, which is consistent with the observed meridian-aligned flare ribbons. The constant tilt angle shows that the CME did not apparently rotate near the Sun. The other three parameters are slightly adjusted according to the data times, and the changes of aspect ratio and half angle could be explained by the expansion of the flux rope. Zuccarello et al. (2012) reported that a CME could be deflected latitudinally about 15° toward the equator within $\sim$3.5 $R_{\odot}$. The roughly constant latitude (around 0°) in Table 1 indicates that the CME in the present work was diverted over 10° southward from the location of source region ($\sim$W62°N15° as indicated with the two vertical lines in Figure 3) before reaching the height of 3 $R_{\odot}$. The GCS modeling results also show that the CME was deflected over 10° eastward at the height of $6.15\,R_{\odot}$. The CME propagation direction at $6.15\,R_{\odot}$ is roughly in the southeast of the source region, which is near the regions of lower magnetic energy density as shown in Figure 3. The deflection direction of the CME in the low corona is roughly consistent with the distribution of the magnetic energy density. The direction variation of the CME revealed by the GCS model is minor above $6.15\,R_{\odot}$ as shown in Table 1, which is consistent with that the rate of CME deflection caused by the coronal magnetic field is more significant within a few solar radii (e.g., Isavnin et al. 2014; Kay et al. 2015).

3. Properties in Interplanetary Space

The interplanetary kinematics of the CME is derived through a geometric triangulation technique initially proposed by Liu et al. (2010a) based on stereoscopic wide-angle imaging observations from *STEREO*. The triangulation method first utilizes a Fixed β (Fβ) geometry for the CME front, which assumes a relatively compact structure (Sheeley et al. 1999; Kahler & Webb 2007) simultaneously observed by two separated spacecraft. Later, Lugaz et al. (2010) and Liu et al. (2010b) incorporated a HM approximation, which assumes that the CME front is a sphere attached to the Sun and tangent to the lines of sight of the two spacecraft. The triangulation concept has proved to work well in acquiring CME interplanetary kinematics and in connecting remote sensing observations with in situ signatures (e.g., Liu et al. 2010a, 2010b, 2013, 2016; Lugaz et al. 2010; Möstl et al. 2010; Harrison et al. 2012; Davies et al. 2013; Hu et al. 2016). The triangulation technique with Fβ and HM approximations is detailed and discussed in Liu et al. (2010b, 2013, 2016).

The elongations and times as inputs of the triangulation method are from the observations of *STEREO* COR2, HI1 and HI2. The angular FOV is $0^{\circ}.7$–4° around the Sun for COR2, $20^{\circ} \times 20^{\circ}$ centered at 14° from the center of the Sun for HI1, and 70° in diameter centered at $53^{\circ}.7$ for HI2 (Howard et al. 2008). The left panel of Figure 5 depicts the running difference images of the CME in interplanetary space taken by HI1 and HI2 of *STEREO A* and *B*. The feature near the northern edge of the CME in the HI1 images might be the substructure of the CME that is also observed by *SOHO*/C2. We cannot rule out the possibility that the feature is of another CME. The

Table 1
Times and Fitted Parameters of GCS Model for the CME

Time (STEREO, UT)	Longitude (Carrington, °)	Longitude (HEE, °)	Latitude (HEE, °)	Height ($R_\odot$)	Aspect Ratio	Half Angle (°)
SOHO/LASCO C2 and STEREO/COR1						
15:25	76.4	60.4	3	3.00	0.3	20
15:35	74.1	58.1	3	3.29	0.3	20
15:45	72.2	56.4	3	3.59	0.3	20
16:00	71.0	55.3	3	4.00	0.3	25
16:10	69.9	54.3	3	4.41	0.3	25
16:25	68.0	52.5	3	4.86	0.3	27
SOHO/LASCO C2 and STEREO/COR2						
16:39	64.9	49.5	2	5.57	0.4	30
16:54	63.3	48.1	2	6.15	0.4	30
17:24	62.9	48.0	2	7.35	0.4	30
SOHO/LASCO C3 and STEREO/COR2						
17:39	62.9	48.1	1	7.79	0.4	30
17:54	62.7	48.1	0	8.40	0.4	30
18:24	62.5	48.1	0	9.71	0.4	33
18:39	62.3	48.1	0	10.28	0.4	33
18:54	62.2	48.1	0	10.79	0.4	33
19:24	60.9	47.1	0	11.81	0.4	35
19:39	60.7	47.0	0	12.71	0.4	35
19:54	60.7	47.1	0	13.56	0.4	35
20:24	59.8	46.5	0	14.85	0.4	35
20:39	59.3	46.1	0	15.64	0.4	35
21:24	58.6	45.8	0	17.57	0.4	35

Note. The times are from the STEREO A data. For each time only the longitude and height are fitted, and the other parameters are fixed and merely adjusted according to the times. The tilt angle is set to 90° (see the text), which is not shown in the table.

northern front of the CME was distorted and the southern part of the front was advancing the other part. Through stacking the running difference intensities of COR2, HI1, and HI2 within a slit along the ecliptic plane, we construct two time-elongation maps (J-maps, e.g., Sheeley et al. 1999) for the CME as shown in the right panel of Figure 5. The red curves in the maps represent the elongation angles of the CME front near the ecliptic plane observed from the viewpoints of STEREO A and B, respectively. STEREO A tracked the CME out to ∼50°, while STEREO B followed the CME out to ∼40°, as indicated by the red curves. The elongations and times are extracted and used as inputs of the triangulation method. The CME kinematics along the ecliptic plane derived from the Fβ and HM triangulations will be compared with the in situ observations. The trajectories of the CME derived from the triangulation with the Fβ and HM approximations, as well as the positions of the spacecraft in the ecliptic plane during the event are displayed in Figure 1. The black diamonds and red crosses in Figure 1 represent the trajectory of the CME apex in the ecliptic plane derived from the Fβ and HM triangulations, respectively. The green and blue circles represent the sizes of the HM assumed spherical front when the CME arrives at Wind and VEX, respectively. The arrows indicate the directions of the apex when the CME arrives the two spacecraft.

The propagation direction, height, and speed of the CME in the ecliptic plane derived from the triangulation method and the kinematics in the corona obtained from the GCS model are presented in Figure 6. In the top panel, the derived propagation direction is given in degrees from the Sun–Earth line. The direction angle acquired from the HM triangulation is roughly twice the one from the Fβ triangulation and more variational, which is noticed in previous studies (Lugaz et al. 2010;

Liu et al. 2013, 2016). Near the Sun, the longitude is overestimated by the HM approximation, which is probably a result of the overestimated CME size as discussed in Liu et al. (2013, 2016). Both the GCS model and the Fβ triangulation reveal that the CME was propagating to the east of the source region, and the direction changed dramatically toward the east in the low corona. The direction angles from the GCS model are between those from the Fβ and HM approximations. The direction angles from the GCS model are closer to those from the Fβ approximation at lower heights and have a trend to approach to those from the HM approximation at larger heights. The CME was deflected from about 60° to about 50° west of the Sun–Earth line below ∼$6\,R_\odot$. The difference between the propagation directions before and after the data gap in the top panel of Figure 6 implies that the CME may continue to turn eastward in interplanetary space. The final propagation direction angle before reaching the Earth is likely around 20° west of the Sun–Earth line, to which both the Fβ and HM triangulations seem to converge. Given these variations in the propagation direction, the CME possibly arrived at Venus (VEX) which was longitudinally ∼90° distant from the source region (see the text below). There were other ejections launched near AR 11103 and 11102 on September 4, which were all on the west side of the CME of interest. One of these ejections may interact with the CME, which is likely to be the reason for the direction change of the CME in interplanetary space. As shown in the middle and bottom panels of Figure 6, the GCS model and the triangulation method give consistent distances and speeds of the CME below ∼$20\,R_\odot$. The distances and speeds from the Fβ approximation slightly deviate from those from the HM approximation beyond ∼$130\,R_\odot$, which is probably due to the limitation of the
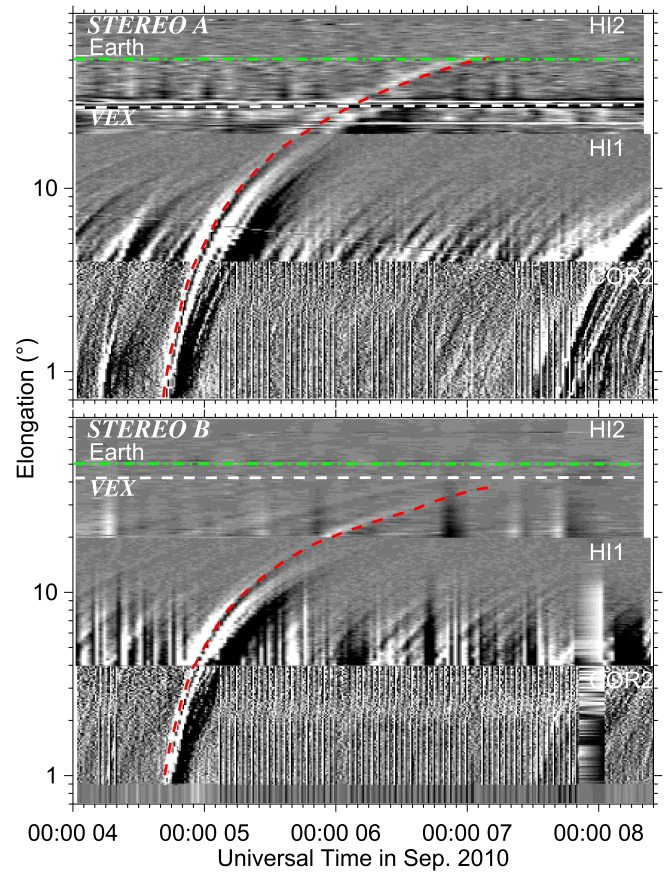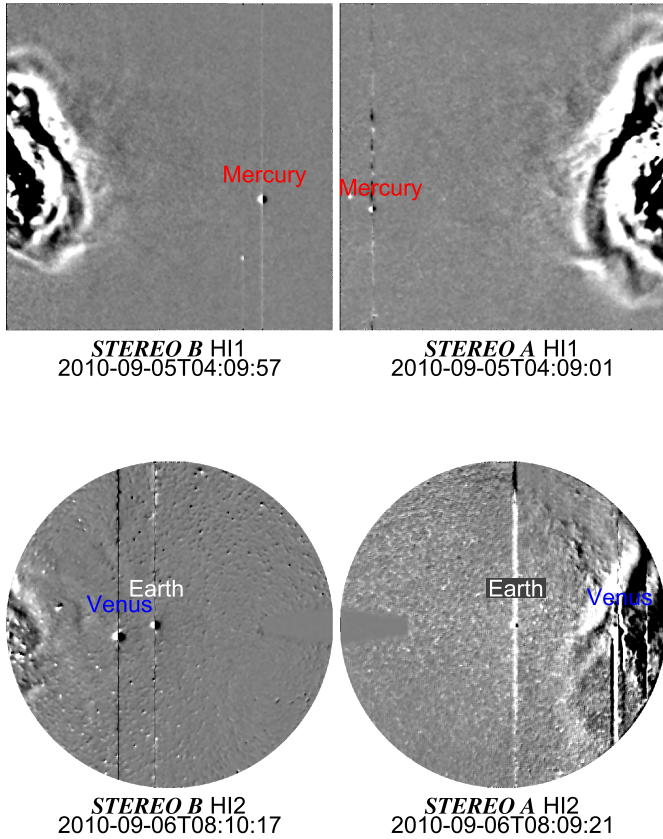
Figure 5. Left: evolution of the CME viewed simultaneously from *STEREO B* and *A*; the top and bottom panels show running difference images from HI1 and HI2, respectively; the positions of Mercury, Venus and the Earth are marked in corresponding HI images. Right: time-elongation maps constructed from running difference images of COR2, HI1, and HI2 along the ecliptic plane for *STEREO A* (upper) and *B* (lower); the red dashed curve indicates the track of the CME, from which the elongation angles of the CME front are extracted; the horizontal lines denote the elongation angles of the Earth (green) and *VEX* (white).

geometric assumption for the Fβ approximation at larger distances as discussed in Liu et al. (2013, 2016). Below $\sim 30\,R_\odot$, the CME was gradually accelerated to about $600\,\mathrm{km\,s^{-1}}$. Due to the data gap, we cannot tell if there is a deceleration process, but the speeds beyond $\sim 60\,R_\odot$ do not show much variation ($\sim 620\,\mathrm{km\,s^{-1}}$ for Fβ approximation and $\sim 530\,\mathrm{km\,s^{-1}}$ for HM approximation as marked in Figure 1).

Figure 7 shows the solar wind magnetic field measurements from the *VEX* magnetometer (Zhang et al. 2006), where the ICME (with an interval of $\sim 7.5\,\mathrm{hr}$ from 11:04 UT to 18:33 UT on September 8) is reported by Good & Forsyth (2016). The high fluctuations of the magnetic field at lower altitudes was probably caused by the induced magnetosphere of Venus. *VEX* was at a distance of $\sim 0.73\,\mathrm{au}$ with a longitude of $\sim -31°$ that was over $90°$ away from the source region. The distance data range of the CME derived from the observed elongations using the triangulation method is not large enough to estimate the arrival times of the CME front at *VEX* and *Wind*. Assuming a fixed propagation direction ($\sim 17°$ from the Sun–Earth line for Fβ and $\sim 24°$ for HM) outside the data range, we use a linear fit of the distances determined by the triangulations to estimate the arrival times of the CME at *VEX* and *Wind*. The HM triangulation suggests that the eastern flank of the CME (the eastern part of the blue circle attached to the Sun in Figure 1) arrived at *VEX* around 15:53 UT on September 8, about 5 hr later than the start time of the ICME observed at *VEX*, with a radial speed at *VEX* of $\sim 310\,\mathrm{km\,s^{-1}}$. Assuming that the compact structure for the Fβ approximation is the dominant

apex and the CME front is also a circle attached to the Sun like the HM approximation, we estimate the arrival time at *VEX*, using the Fβ derived directions and distances, to be 20:52 UT on September 7, about 14 hr earlier than the observed ICME start time. The HM triangulation has well predicted the arrival times of ICMEs in comparison to the in situ observed start times of the ICMEs (e.g., Liu et al. 2010b, 2016). In our case, the small difference between the HM triangulation derived arrival times and the ICME start time suggests that the *VEX* observed ICME shown in Figure 7 is the interplanetary counterpart of the CME of interest.

The associated in situ measurements at *Wind* during the event are displayed in Figure 8. Two ICME-like structures are indicated with "I1" and "I2" in the figure, one of which may be associated with the CME of interest. Although the alpha-to-proton density ratio is below the threshold for a typical ICME (e.g., Richardson & Cane 2004; Liu et al. 2005), the duration of structure I1 ($\sim 6\,\mathrm{hr}$ from 19:42 UT on September 7 to 1:39 UT on September 8) can be determined by a combination of the increase of the alpha-to-proton density ratio, the low proton temperature (Richardson & Cane 1995), and the magnetic field profile. Structure I2 has an interval of $\sim 15.5\,\mathrm{hr}$ (from 10:15 UT on September 8 to 1:52 UT on September 9), whose trailing edge may be ambiguous. The HM approximation determines the arrival time of the CME at *Wind* to around 03:23 UT on September 8 and the estimated radial speed is $\sim 490\,\mathrm{km\,s^{-1}}$. The F$\beta$ approximation gives an arrival time around 18:17 UT on September 7. The HM estimated arrival time is $\sim 8\,\mathrm{hr}$ later
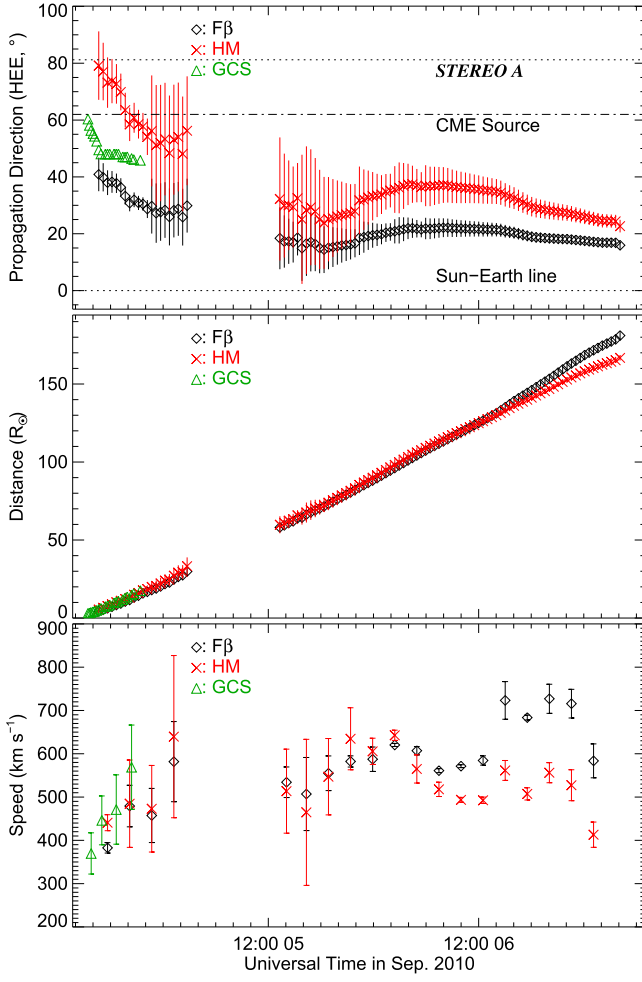
Figure 6. Propagation direction, radial distance, and speed profiles of the apex of the CME front derived from the GCS model (green triangle), and the triangulation method with the Fβ (black diamond) and HM (red cross) approximations. The Sun–Earth line, and longitudes of *STEREO A* and the source region of the CME, are indicated by the horizontal lines in the top panel. The speeds are calculated from adjacent distances using a numerical differentiation with three-point Lagrangian interpolation and are then binned to reduce the scatter. The data gap is due to singularities in the calculation scheme caused by the spacecraft longitudinal separation angle (Liu et al. 2011).

Figure 7. Magnetic field measurements at *VEX* and the field angles in the RTN system. Also shown are the position of the spacecraft in VSO coordinates and the altitude from the center of Venus. The two vertical dashed lines mark the ICME interval from Good & Forsyth (2016). The high fluctuations of the magnetic field at lower altitudes was probably caused by the induced magnetosphere of Venus.

than the start time of structure I1, and is ∼7 hr earlier than the start time of I2. The Fβ estimated arrival time is ∼1 hr earlier than the start time of I1, and is ∼16 hr earlier than the start time of I2. Given the small difference between the estimated and observed arrival times, it is difficult to determine which of the two ICME-like structures (I1 and I2) is associated with the CME of interest. There was a brief structure (from 12:18 UT to 16:26 UT on September 9) after structure I2, which is likely irrelevant to the CME of interest because of its late start time.

Figure 9 shows the in situ measurements at *STEREO A* during the event. On September 7, *STEREO A* observed a shock leading an ICME with the arrival time of 8:29 UT. The ICME interval is from around 13:00 UT on September 7 to around 9:45 UT on September 8, which is determined from the combination of the low-temperature region and magnetic field profile. Both the shock arrival time and the ICME start time are over 80 (60) hr earlier than the Fβ (HM) estimated arrival time. Although the triangulation assumed shape may deviate from the real geometry of the CME, the large difference between the estimated and observed arrival times can hardly associate the
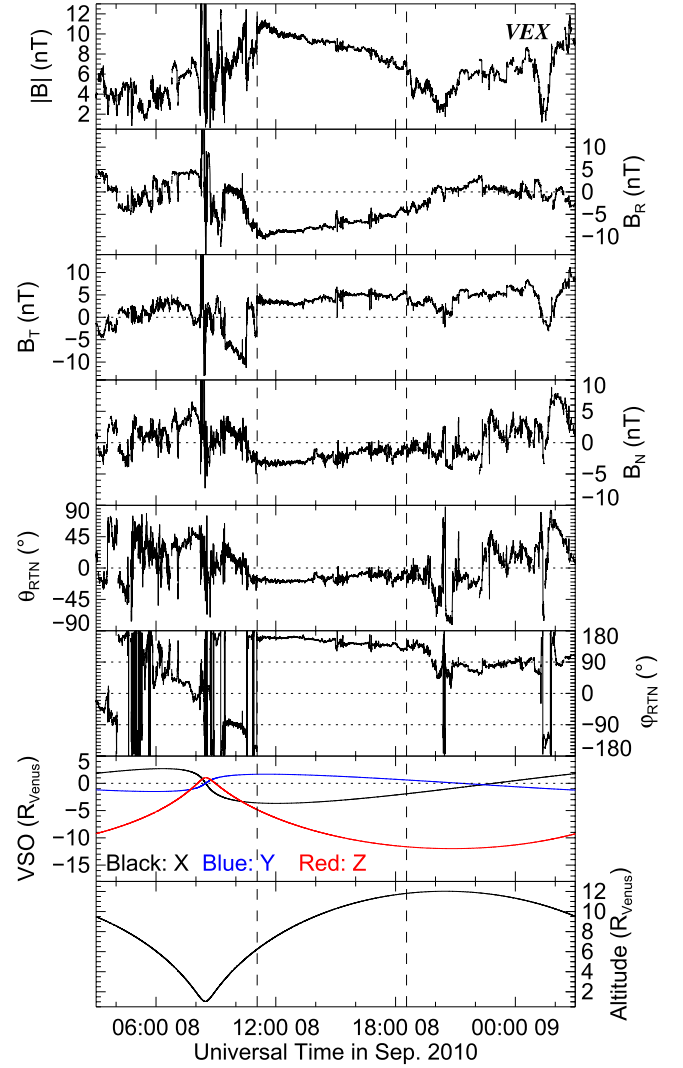
STEREO A observed ICME with the CME of interest. This is also consistent with the statement in the ICME catalog of Good & Forsyth (2016) that no in situ ICME signatures observed at *STEREO A* were likely to be associated with the ICME at *VEX* in Figure 7. A couple of ejections were launched from source regions longitudinally close to *STEREO A* on September 4. The *STEREO A* observed ICME might be associated with one of these ejections, which might interact with the CME of interest and caused the latter to continue turning eastward in interplanetary space.

The HM approximation estimated arrival times of the CME at *VEX* and *Wind* are generally consistent with the observed, even though the ICME at *Wind* cannot be uniquely associated with the CME of interest. This seems to suggest that the assumed spherical geometry is applicable to the eastern part of the CME front in this case. The in situ measurements and the triangulation method both reveal that the arrival time of the CME at Venus (*VEX*) is not earlier than that at the Earth (*Wind*), although the Sun–Venus distance (∼0.73 au) was less
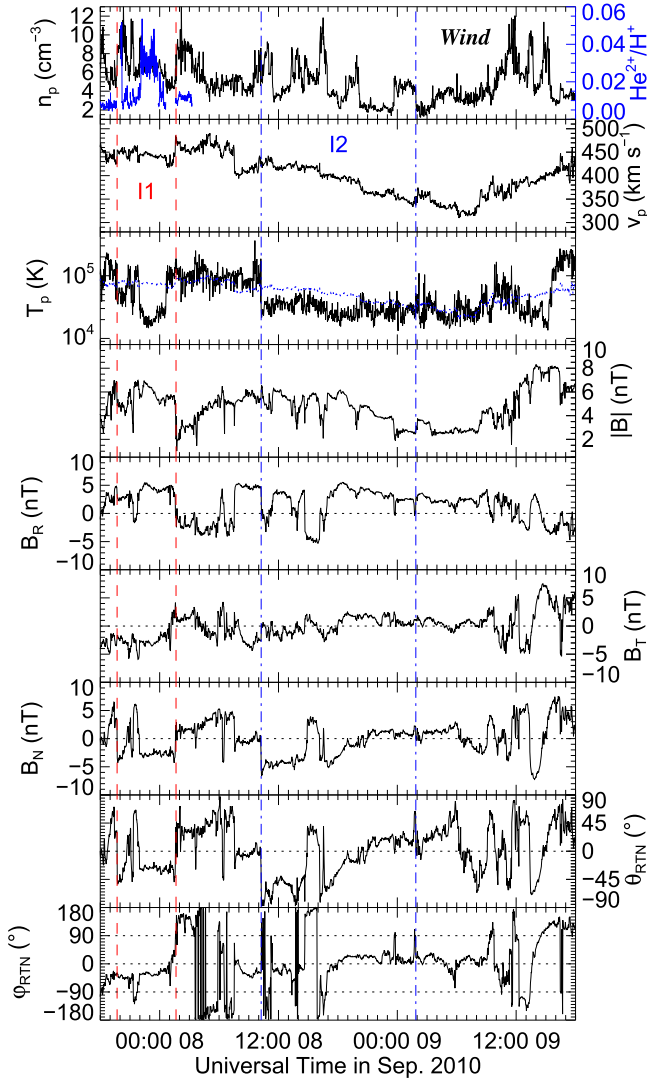
Figure 8. Solar wind plasma and magnetic field parameters during the event measured at *Wind*. From top to bottom, the panels show the proton density (with the alpha-to-proton density ratio from *ACE* overlaid in blue), bulk speed, proton temperature (overlaid with the expected proton temperature calculated from the observed speed (Lopez 1987)), magnetic field strength, components, and field angles in the RTN system, respectively. The red and blue vertical lines indicate the intervals of two ICME-like structures that are marked with "I1" and "I2," respectively.

Figure 9. An ICME driving a shock observed by *STEREO A*. The panels are similar to those of Figure 8. The red vertical line marks the arrival time of the shock, and the two black vertical lines indicate the interval of the ICME.

than the Sun–Earth distance. This is exactly what is shown in Figure 1: the expanding eastern flank of the assumed CME circle touches *VEX* after the front reaches *Wind*. Therefore, the arrival times of the CME at the two spacecraft with different heliocentric distances can be determined by the joint effect of the propagation direction and the assumed expanding circular shape. However, it is unclear whether the assumed shape could describe the geometry of the western part of the CME because of the lack of consistent in situ measurement of the western part. Assuming that the CME front is symmetric with respect to the final propagation direction, we estimate the longitudinal angular width of the CME front to be probably no less than 100° given that the angular distance between *VEX* and the propagation direction is ∼50°. Let the semi-perimeter of the circle (the leading edge of the flux rope) in the HM approximation represent the longitudinal transverse size, and we estimate the size to be ∼1.7 au when the CME arrived at
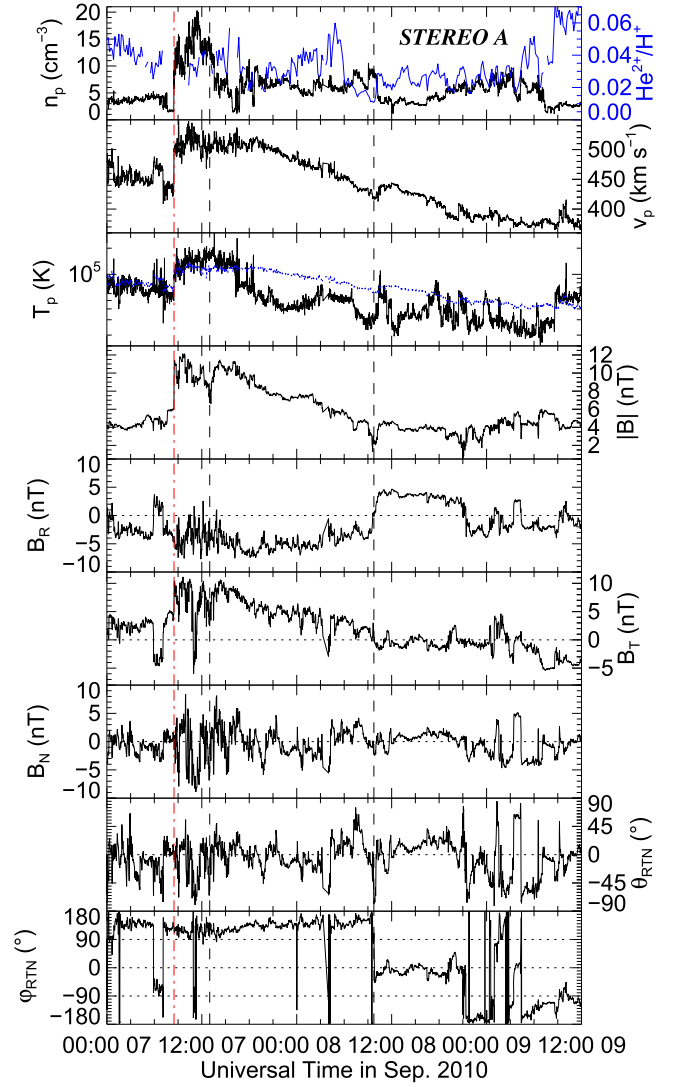
Wind. The radial widths of structures I1 and I2 at *Wind* (as indicated in Figure 8), obtained from the HM estimated radial speeds multiplied by the durations, are ∼0.07 au and ∼0.18 au, respectively. Both the radial widths of structures I1 and I2 are far less than the transverse size ∼1.7 au. Note that the flux rope is generally perpendicular to the ecliptic plane as can be seen from Section 2, so the transverse size is approximately equal to the transverse size of the cross section of the flux rope in the ecliptic plane. This result suggests that the ICME structure was extremely compressed in the radial direction and extended in the longitudinal direction in interplanetary space.

4. Conclusions and Discussion

We investigated a CME launched on 2010 September 4 from a source region connecting AR 11101 and AR 11103, based on EUV, magnetogram, white-light and in situ observations from *SDO*, *STEREO*, *SOHO*, *VEX*, and *Wind*. The PFSS model is used to examine the magnetic field environment near the source region. The GCS model and the triangulation method are applied to analyze the kinematics and structure in the corona and interplanetary space. Below, we summarize the results and

discuss their crucial implications for understanding (1) how the propagation direction of the CME in the low corona is changed by the asymmetric magnetic field configuration caused by the ARs on one side of the source region; (2) the determination of both the CME frontal shape and the propagation direction in space weather forecasting; and (3) the deformation of the ICME structure.

1. The CME was deflected in the low corona by the magnetic pressure from the two nearby ARs in the west, and possibly interacted with another CME in interplanetary space. The erupting flux rope originated from the positive and negative polarity regions belonging to the two different ARs. With all the sunspots on the west side, the source region was adjacent to the eastern edges of the two ARs, which caused an asymmetric magnetic field configuration on the two sides of the eruption and resulted in a deflection of the CME in the low corona. The deflection direction revealed by the GCS model is consistent with the general direction of the gradient descent of the magnetic energy density derived from the PFSS model. This suggests that a CME originated from the edge of an AR is likely to be deflected toward a non-radial motion due to the asymmetric background magnetic field configuration. This is similar to the case of Möstl et al. (2015) and Wang et al. (2015), where the strong magnetic field on one side of the CME source region changed the propagation direction of the CME. However, a CME–CME interaction is possibly involved in the change of propagation direction. Given that there were other ejections with close launch times and source regions to those of the CME of interest, the CME possibly interacted with one of these ejections during the propagation. The deflection and interaction may be the reason that caused the CME to reach *VEX* that was longitudinally distant from the source region. CME–CME interaction is not unusual and may change the propagation direction and 1 au property of a CME (e.g., Gopalswamy et al. 2001; Lugaz et al. 2009, 2012; Liu et al. 2012, 2014, 2015). This illustrates the necessity of considering both the background magnetic field condition and successive eruptions near the source region in determining the propagation direction of a CME.

2. It is important to determine both the frontal shape and the propagation direction of the CME in interplanetary space for space weather forecasting. Although the associated ICME at *Wind* cannot be uniquely identified from the two plausible structures, the HM triangulation with a circular geometry in the ecliptic plane can give arrival times that are less than 8 hr different from observed at *VEX* and *Wind*. Both the observed and the triangulation estimated arrival times of the CME at *VEX* (∼0.73 au) are not earlier than those at *Wind* (∼1 au), although *VEX* was closer to the Sun than *Wind*. These results suggest that the simple expanding sphere attached to the Sun may describe the shape of the eastern CME front in the inner heliosphere. However, the spherical shape is only consistent with in situ measurements at two points, and there is no consistent observations of the western part of the CME. The real geometry of the CME front is not strongly constrained. Furthermore, the CME could be distorted to a complex geometry so that it arrived at *VEX* later. Also note that the HM triangulation gives a misleading propagation direction near the Sun and large variations in the propagation direction. The CME touched *VEX* with its eastern flank in this case, and the flank of a CME could also trigger a geomagnetic storm as reported by Möstl et al. (2010). This indicates the importance of determining both the CME frontal shape and propagation direction in forecasting geomagnetic activity.

3. The structure of the CME in interplanetary space was compressed radially and extended longitudinally, leading to a large transverse size of the flux-rope cross section in the ecliptic plane. An estimate of the transverse size and deformation of the ICME structure in the inner heliosphere could be helpful to improve our knowledge of the interaction between the ICME and the solar wind as well as space weather forecasting. For example, the transverse size can increase the contact area of the interaction between an ICME and the solar wind and the probability of arriving at the Earth, while the deformation could alter the plasma and magnetic field properties of an ICME near the Earth. Observations from the *Solar Orbiter* (Müller et al. 2013) out of the ecliptic plane can be of great advantage to study the kinematics and geometric evolution of CMEs, as well as their interactions with other structures in the solar wind.

References

Amari, T., Luciani, J. F., Mikic, Z., & Linker, J. 2000, ApJL, 529, L49
Cheng, X., Ding, M. D., Zhang, J., et al. 2014, ApJ, 789, 93
Cremades, H., & Bothmer, V. 2004, A&A, 422, 307
Davies, J. A., Harrison, R. A., Perry, C. H., et al. 2012, ApJ, 750, 23
Davies, J. A., Perry, C. H., Trines, R. M. G. M., et al. 2013, ApJ, 777, 167
Domingo, V., Fleck, B., & Poland, A. I. 1995, SoPh, 162, 1
Good, S. W., & Forsyth, R. J. 2016, SoPh, 291, 239
Gopalswamy, N., Mäkelä, P., Xie, H., Akiyama, S., & Yashiro, S. 2009, JGRA, 114, A00A22
Gopalswamy, N., Yashiro, S., Kaiser, M. L., Howard, R. A., & Bougeret, J.-L. 2001, ApJL, 548, L91
Gopalswamy, N., Yashiro, S., Krucker, S., Stenborg, G., & Howard, R. A. 2004, JGRA, 109, A12105
Gopalswamy, N., Yashiro, S., Michalek, G., et al. 2005, GeoRL, 32, L12S09
Harrison, R. A., Davies, J. A., Möstl, C., et al. 2012, ApJ, 750, 45
Howard, R. A., Moses, J. D., Vourlidas, A., et al. 2008, SSRv, 136, 67
Hu, H., Liu, Y. D., Wang, R., Möstl, C., & Yang, Z. 2016, ApJ, 829, 97
Isavnin, A., Vourlidas, A., & Kilpua, E. K. J. 2014, SoPh, 289, 2141
Jin, M., Schrijver, C. J., Cheung, M. C. M., et al. 2016, ApJ, 820, 16
Kahler, S. W., & Webb, D. F. 2007, JGRA, 112, 9103
Kaiser, M. L., Kucera, T. A., Davila, J. M., et al. 2008, SSRv, 136, 5
Kataoka, R., Shiota, D., Kilpua, E., & Keika, K. 2015, GeoRL, 42, 5155
Kay, C., Opher, M., & Evans, R. M. 2013, ApJ, 775, 5
Kay, C., Opher, M., & Evans, R. M. 2015, ApJ, 805, 168
Kilpua, E. K. J., Pomoell, J., Vourlidas, A., et al. 2009, AnGeo, 27, 4491
Lemen, J. R., Title, A. M., Akin, D. J., et al. 2012, SoPh, 275, 17
Liewer, P., Panasenco, O., Vourlidas, A., & Colaninno, R. 2015, SoPh, 290, 3343
Liu, Y., Davies, J. A., Luhmann, J. G., et al. 2010a, ApJL, 710, L82
Liu, Y., Luhmann, J. G., Bale, S. D., & Lin, R. P. 2011, ApJ, 734, 84
Liu, Y., Richardson, J. D., & Belcher, J. W. 2005, P&SS, 53, 3
Liu, Y., Richardson, J. D., Belcher, J. W., et al. 2006, JGRA, 111, A12S03
Liu, Y., Thernisien, A., Luhmann, J. G., et al. 2010b, ApJ, 722, 1762
Liu, Y. D., Hu, H., Wang, C., et al. 2016, ApJS, 222, 23
Liu, Y. D., Hu, H., Wang, R., et al. 2015, ApJL, 809, L34
Liu, Y. D., Luhmann, J. G., Kajdič, P., et al. 2014, NatCo, 5, 3481

Liu, Y. D., Luhmann, J. G., Lugaz, N., et al. 2013, ApJ, 769, 45
Liu, Y. D., Luhmann, J. G., Möstl, C., et al. 2012, ApJL, 746, L15
Lopez, R. E. 1987, JGR, 92, 11189
Lugaz, N., Farrugia, C. J., Davies, J. A., et al. 2012, ApJ, 759, 68
Lugaz, N., Hernandez-Charpak, J. N., Roussev, I. I., et al. 2010, ApJ, 715, 493
Lugaz, N., Vourlidas, A., & Roussev, I. I. 2009, AnGeo, 27, 3479
MacQueen, R. M., Hundhausen, A. J., & Conover, C. W. 1986, JGR, 91, 31
Manchester, W. B., Gombosi, T. I., Roussev, I., et al. 2004, JGRA, 109, 2107
Möstl, C., & Davies, J. A. 2013, SoPh, 285, 411
Möstl, C., Rollett, T., Frahm, R. A., et al. 2015, NatCo, 6, 7135
Möstl, C., Temmer, M., Rollett, T., et al. 2010, GeoRL, 37, 24103
Müller, D., Marsden, R. G., St., Cyr, O. C., & Gilbert, H. R. 2013, SoPh, 285, 25
Odstrcil, D., Riley, P., & Zhao, X. P. 2004, JGRA, 109, 2116
Panasenco, O., Martin, S. F., Velli, M., & Vourlidas, A. 2013, SoPh, 287, 391
Qiu, J., Wang, H., Cheng, C. Z., & Gary, D. E. 2004, ApJ, 604, 900
Richardson, I. G., & Cane, H. V. 1995, JGR, 100, 23397
Richardson, I. G., & Cane, H. V. 2004, JGRA, 109, A09104
Riley, P., Linker, J. A., Mikić, Z., et al. 2003, JGRA, 108, 1272
Rollett, T., Möstl, C., Isavnin, A., et al. 2016, ApJ, 824, 131
Savani, N. P., Owens, M. J., Rouillard, A. P., Forsyth, R. J., & Davies, J. A. 2010, ApJL, 714, L128
Schou, J., Scherrer, P. H., Bush, R. I., et al. 2012, SoPh, 275, 229
Schrijver, C. J., & Title, A. M. 2011, JGRA, 116, A04108
Sheeley, N. R., Walters, J. H., Wang, Y.-M., & Howard, R. A. 1999, JGR, 104, 24739
Thernisien, A., Vourlidas, A., & Howard, R. A. 2009, SoPh, 256, 111
Thernisien, A. F. R., Howard, R. A., & Vourlidas, A. 2006, ApJ, 652, 763
Wang, R., Liu, Y. D., Dai, X., et al. 2015, ApJ, 814, 80
Xie, H., St., Cyr, O. C., Gopalswamy, N., et al. 2009, SoPh, 259, 143
Zhang, J., Cheng, X., & Ding, M.-D. 2012, NatCo, 3, 747
Zhang, T. L., Baumjohann, W., Delva, M., et al. 2006, P&SS, 54, 1336
Zuccarello, F. P., Bemporad, A., Jacobs, C., et al. 2012, ApJ, 744, 66